



THE PREDICTION OF A SIZE EFFECT IN MICRO-INDENTATION

J. Y. SHU

Chemistry and Materials Science Department, Lawrence Livermore National Laboratory,
Livermore, CA 94551, U.S.A.

and

N. A. FLECK

Cambridge University Engineering Department, Trumpington Street, Cambridge,
CB2 1PZ, U.K.

E-mail: naf1@eng.cam.ac.uk

(Received 17 September 1996; in revised form 24 March 1997)

Abstract—The indentation hardness of metals depends upon the size of the indent, for indents in the size range of 0.1–10 μm . A finite element method is used to predict this size effect, based on Fleck–Hutchinson strain gradient plasticity theory. The material is treated as a power law, deformation theory solid such that the strain energy density depends upon both strain and strain gradient. An indentation size effect is predicted for axisymmetric indenters of various head-shape (flat, conical and spherical), and the role of contact friction is explored. It is found that the predicted hardness increases significantly when the size of the indent is comparable to the material micro-length scale.
© 1998 Elsevier Science Ltd.

1. INTRODUCTION

Indentation tests have been widely used as an economical, routine method for measuring the strength of engineering materials. A range of head-shapes are used including a sphere (Brinell test), a circular one (Rockwell C), a three-sided pyramid (Berkovich) and a four-sided pyramid (Vickers): in all cases the hardness is defined as the total load on the indenter divided by the projected contact area A . It is convenient to refer to the size of an indent by the radius $a = \sqrt{A/\pi}$ of a circle which has the same area, A , as the projected area of contact for the physical indenter, at a given indentation depth h . Conventional plasticity theory contains no internal length scale and thereby predicts no size effect. This is consistent with the observation that the indentation strength of metals is found to be independent of the indent size for a greater than about 10 μm . However, when a is reduced from 10 μm to about 0.1 μm the measured hardness increases typically by a factor of 2–3 for pure metals and alloys. For example, Ma and Clarke (1994) conducted indentation tests on a silver single crystal using a Berkovich indenter. The hardness was found to almost double when the indent size a was reduced from 10 to 1 μm . Poole *et al.* (1995) reported a comparable size effect for indentation of pure copper by a Vickers indenter.

Similar size effects have been observed for a wide range of plasticity phenomena. For example, both the yield strength and the strain hardening rate of metals increase with diminishing grain size. The strength of particle-reinforced metals increases with diminishing particle diameter at a fixed volume fraction (Kelly and Nicholson, 1963; Ebeling and Ashby, 1966). New constitutive theories involving a material length are needed in order to characterize and predict such phenomena. Recently, a strain gradient theory has been proposed by Fleck *et al.* (1994) and Fleck and Hutchinson (1993). The theory is based on the notion that the yield strength of a metal depends upon the total density of geometrically necessary and statistically stored dislocations. The density of geometrically necessary dislocations scales with the magnitude of the strain gradient and the density of statistically stored dislocation scales with the effective strain. Dimensional considerations dictate that a material length scale ℓ be present in the constitutive law, and the theory fits within the

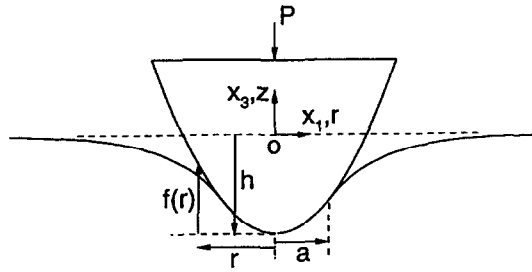


Fig. 1. Indentation of a half space by an axisymmetric indenter, with notation and sign conventions. The head-shape of the indenter is defined by $f(r)$, and the contact extends over a radius a for a given indentation depth h .

framework of reduced couple stress theory. The precise physical interpretation of the material length scale remains unclear, but it may be interpreted loosely as the mean free path of dislocations. A number of practical problems have been explored using this constitutive law including the stress field in the vicinity of a hole and in the vicinity of a particle (Fleck and Hutchinson, 1993), and the stress field near a crack tip (Xia and Hutchinson, 1996). Recently, Fleck and Hutchinson (1997) have introduced a more general version of their strain gradient theory in which hardening is due to all components of the spatial gradient of strain: the contribution to strengthening from stretch gradients is included in addition to the contribution from curvature of the deformation field.

In the current article, the Fleck–Hutchinson strain gradient plasticity theory is implemented using a finite element method and is used to estimate the observed size dependence of the indentation hardness of metals. A half-space made from a power-law deformation theory solid is indented by an axisymmetric, rigid indenter of head shape

$$f(r) = \frac{r^m}{D^{m-1}} \quad (1)$$

as defined in Fig. 1. Here, r is the radial co-ordinate of a cylindrical co-ordinate system (r, θ, z) , D is the leading dimension of the indenter, and m describes the shape of the indenter. For example, $m = \infty$ represents a flat-ended punch of diameter D ; $m = 2$ indicates a ball of diameter D ; a conical indenter with an included tip angle of 2β is defined by $m = 1$ and $D^{m-1} = \tan\beta$. It is found that the predicted hardness approaches that given by conventional theory when the indent size is much larger than the material length scale; however, the predicted hardness is elevated significantly when the indent size is comparable to the material length scale. Preliminary calculations show that the increase in hardness with increasing friction is greater for a strain gradient theory solid than for a conventional solid.

2. REVIEW OF STRAIN GRADIENT THEORY

2.1. Equilibrium and kinematics

The strain gradient theory proposed by Fleck *et al.* (1994), Cosserat and Cosserat and by Fleck and Hutchinson (1993) falls within the classification of reduced couple stress theory. The pertinent kinematic quantities in reduced couple stress theory are the material displacement \mathbf{u} and the associated material rotation $\boldsymbol{\theta} \equiv (1/2) \text{curl} \mathbf{u}$. However, for the purposes of numerical computation we shall restate the strain gradient theory of Fleck *et al.* (1994) in terms of general couple stress theory, and introduce a micro-rotation, $\boldsymbol{\omega}$, which is distinct from the material rotation, $\boldsymbol{\theta}$. The micro-rotation, $\boldsymbol{\omega}$, is treated as an independent kinematic quantity with no direct dependence upon \mathbf{u} ; this enables the use of C_0 -continuous elements in a finite element formulation, as detailed below.

We begin by outlining general couple stress theory and show how it degenerates to reduced couple stress theory upon identifying the rotation $\boldsymbol{\omega}$ with the material rotation $\boldsymbol{\theta}$. In both the general and reduced versions of couple stress theory it is supposed that a

material point can support couple stress (bending moment per unit area) in addition to Cauchy stress. The presence of couple stresses implies that the Cauchy stress tensor is unsymmetric. Denote the Cauchy stress tensor by the sum of a symmetric part σ and an anti-symmetric part τ , and denote the couple stress tensor by m . Force equilibrium at each point within the volume V of the body dictates

$$\sigma_{ij,i} + \tau_{ij,j} = 0 \tag{2}$$

and moment equilibrium implies

$$\tau_{ij} = \frac{1}{2} - e_{ijk} m_{nk,n}. \tag{3}$$

Here, we adopt the standard notation that a comma indicates a partial derivative with respect to a Cartesian co-ordinate, and a repeated suffix denotes summation over 1 to 3. A subscript index can take the value of 1, 2, or 3 and e_{ijk} is the usual permutation symbol. Traction equilibrium on the surface S of the body gives

$$(\sigma_{ij} + \tau_{ij})n_i = T_j \quad \text{and} \quad m_{ij}n_i = Q_j \tag{4}$$

where T_j is surface traction per unit area and Q_j is the surface torque per unit area ; n_i is the i th component of the unit normal vector \mathbf{n} at the surface of the body.

The principle of virtual work for a general couple stress theory reads

$$\int_V [(\sigma_{ij} + \tau_{ij})\delta\gamma_{ji} + m_{ij}\delta\chi_{ji}] dV = \int_S [T_j\delta u_j + Q_j\delta\omega_j] dS \tag{5}$$

where the ‘‘relative strain’’ is $\gamma_{ij} \equiv u_{i,j} + e_{ijk}\omega_k$ and the ‘‘micro-curvature’’ is $\chi_{ij} \equiv \omega_{i,j}$. The above virtual work statement can be rearranged to the form

$$\int_V [\sigma_{ij}\delta\varepsilon_{ij} + m_{ij}\delta\chi_{ji} + \tau_{ij}\delta\alpha_{ji}] dV = \int_S [T_j\delta u_j + Q_j\delta\omega_j] dS \tag{6}$$

where the components of the strain tensor ε are $\varepsilon_{ij} = (u_{i,j} + u_{j,i})/2$ and the anti-symmetric tensor α is defined by $\alpha_{ij} \equiv e_{ijk}\omega_k - (u_{j,i} - u_{i,j})/2 = e_{ijk}\omega_k - e_{ijk}\theta_k$. Note that α is a ‘‘relative rotation’’ and is a measure of the difference between the micro-rotation ω and macroscopic material rotation θ ; α vanishes for the particular choice $\omega = \theta \equiv (1/2)\text{curl}\mathbf{u}$. It is evident from eqn (6) that the anti-symmetric component of the Cauchy stress τ is the work conjugate of the relative rotation increment $\delta\alpha$. In the case of reduced couple stress theory the micro-rotation ω is identified with the material rotation θ , α vanishes, and the principle of virtual work simplifies to

$$\int_V [\sigma_{ij}\delta\varepsilon_{ij} + m_{ij}\delta\chi_{ji}] dV = \int_S (T_j\delta u_j + Q_j\delta\theta_j) dS. \tag{7}$$

2.2. Constitutive law

We consider indentation of a half-space made from a deformation theory, incompressible solid as proposed by Fleck *et al.* (1994) and Fleck and Hutchinson (1993). The strain energy density w is assumed to depend upon the combined strain measure

$$\mathcal{E} \equiv (\varepsilon_e^2 + \ell^2\chi_e^2)^{1/2} \tag{8}$$

where $\varepsilon_e \equiv ((2/3)\varepsilon_{ij}\varepsilon_{ij})^{1/2}$ is the usual von Mises effective strain measure and $\chi_e \equiv ((2/3)\chi_{ij}\chi_{ij})^{1/2}$ is the analogous effective curvature. The existence of a material length scale ℓ is demanded

by dimensional considerations. The overall effective stress measure Σ , deviatoric stress $s_{ij} \equiv \sigma_{ij} - (1/3)\delta_{ij}\sigma_{kk}$ and couple stress m_{ij} are defined as the work conjugates of \mathcal{E} , ε_{ij} and χ_{ij} , respectively, giving

$$\delta w = \Sigma \delta \mathcal{E} = s_{ij} \delta \varepsilon_{ij} + m_{ji} \delta \chi_{ij}. \quad (9)$$

Hence,

$$s_{ij} = \frac{2}{3} \frac{\Sigma}{\mathcal{E}} \varepsilon_{ij} \quad \text{and} \quad m_{ij} = \frac{2}{3} \frac{\Sigma}{\mathcal{E}} \chi_{ji}. \quad (10)$$

Substitution of eqn (10) into eqn (8) gives an explicit expression for Σ in terms of the effective stress $\sigma_e = \sqrt{(3/2)s_{ij}s_{ij}}$ and the effective couple stress $m_e = \sqrt{(3/2)m_{ij}m_{ij}}$

$$\Sigma^2 = \sigma_e^2 + \ell^{-2} m_e^2. \quad (11)$$

For the indentation problem it proves convenient to assume the power-law strain hardening law

$$\frac{\mathcal{E}}{\varepsilon_0} = \left(\frac{\Sigma}{\sigma_0} \right)^n \quad (12)$$

which, for the state of universal tension, reduces to

$$\frac{\varepsilon}{\varepsilon_0} = \left(\frac{\sigma}{\sigma_0} \right)^n. \quad (13)$$

Here, σ and ε denote tensile stress and strain, respectively, n is the strain hardening index, σ_0 is a representative yield stress and ε_0 is the associated yield strain.

The above constitutive law (10)–(12) proves convenient in simplifying the moving-boundary problem of indentation by a curved indenter to that of indentation over a fixed contact area. The reduction method makes use of a similarity transform as laid down by Hill *et al.* (1989); this similarity transform is detailed below.

3. SIMILARITY TRANSFORM

Consider indentation of a half space by a curved axisymmetric punch of head profile specified by eqn (1). At a given stage of indentation, the indentation depth is h and the contact radius is a (see Fig. 1). The contact conditions on the plane $x_3 = 0$ are

$$u_3 = -h + r^m / D^{m-1} \quad r < a \quad (14)$$

and

$$\sigma_{33} = \sigma_{31} + \tau_{31} = \sigma_{32} + \tau_{32} = m_{33} = m_{31} = m_{32} = 0 \quad r > a. \quad (15)$$

The additional boundary conditions are

$$\sigma_{31} + \tau_{31} = \sigma_{32} + \tau_{32} = m_{33} = m_{31} = m_{32} = 0 \quad r < a \quad (16)$$

for a frictionless punch and

$$u_1 = u_2 = \omega_1 = \omega_2 = \omega_3 = 0 \quad r < a \quad (17)$$

for a sticking punch. Both the Cauchy stress σ and the couple stress m vanish at infinity.

It proves convenient to scale the co-ordinates and the deformation variables by the following transformation :

$$\tilde{x}_i = x_i/a \quad \tilde{r} = r/a \quad \tilde{\ell} = \ell/a \quad \tilde{h} = h/a \quad (18)$$

$$\tilde{u}_i = (D/a)^{m-1} u_i/a \quad \tilde{\omega}_i = (D/a)^{m-1} \omega_i \quad (19)$$

$$\tilde{\varepsilon}_{ij} = (D/a)^{m-1} \varepsilon_{ij} \quad \tilde{\ell} \tilde{\chi}_{ij} = (D/a)^{m-1} \ell \chi_{ij} \quad (20)$$

and the stresses according to

$$\tilde{\sigma}_{ij} = [(D/a)^{m-1} \varepsilon_0]^{1/n} \sigma_{ij}/\sigma_0 \quad \tilde{\ell}^{-1} \tilde{m}_{ij} = [(D/a)^{m-1} \varepsilon_0]^{1/n} \ell m_{ij}/\sigma_0 \quad (21)$$

$$\tilde{\tau}_{ij} = [(D/a)^{m-1} \varepsilon_0]^{1/n} \tau_{ij}/\sigma_0. \quad (22)$$

Consequently, the equilibrium relations (2) and (3) become

$$\frac{\partial \tilde{\sigma}_{ij}}{\partial \tilde{x}_i} + \frac{\partial \tilde{\tau}_{ij}}{\partial \tilde{x}_i} = 0 \quad \text{and} \quad \tilde{\tau}_{ij} = \frac{1}{2} e_{ijk} \frac{\partial \tilde{m}_{nk}}{\partial \tilde{x}_n} \quad (23)$$

respectively. The constitutive law of eqn (10) transforms to

$$\tilde{s}_{ij} = (2/3) \tilde{\Sigma}^{1-n} \tilde{\varepsilon}_{ij} \quad \tilde{\ell}^{-1} \tilde{m}_{ij} = (2/3) \tilde{\Sigma}^{1-n} \tilde{\ell} \tilde{\chi}_{ji} \quad (24)$$

where $\tilde{\Sigma} = \{3(\tilde{s}_{ij}\tilde{s}_{ij} + \tilde{\ell}^{-2}\tilde{m}_{ij}\tilde{m}_{ij})/2\}^{1/2}$, $\tilde{s}_{ij} = \tilde{\sigma}_{ij} - \delta_{ij}\tilde{\sigma}_{kk}/3$ and $\tilde{\varepsilon}_{ij} = \tilde{\varepsilon}_{ij} - \delta_{ij}\tilde{\varepsilon}_{kk}/3$. Here, the transformed strains $\tilde{\varepsilon}_{ij}$ and micro curvatures $\tilde{\chi}_{ij}$ satisfy the familiar relations

$$\tilde{\varepsilon}_{ij} = \frac{1}{2} \left(\frac{\partial \tilde{u}_i}{\partial \tilde{x}_j} + \frac{\partial \tilde{u}_j}{\partial \tilde{x}_i} \right) \quad \tilde{\chi}_{ij} = \frac{\partial \tilde{\omega}_i}{\partial \tilde{x}_j}. \quad (25)$$

The overall equivalent strain $\tilde{\varepsilon}_e$, von Mises strain ε_e and equivalent curvature χ_e are scaled in an identical fashion to that specified in eqn (20) for the strain measures ε_{ij} and χ_{ij} .

The boundary conditions on the plane $\tilde{x}_3 = 0$ can be restated in transformed variables as

$$\tilde{u}_3 = (1/c^m) - \tilde{r}^m \quad \text{where} \quad c^m = a^m/(hD^{m-1}) \quad \tilde{r} \leq 1 \quad (26)$$

and

$$\tilde{\sigma}_{33} = \tilde{\sigma}_{31} + \tilde{\tau}_{31} = \tilde{\sigma}_{32} + \tilde{\tau}_{32} = \tilde{m}_{33} = \tilde{m}_{31} = \tilde{m}_{32} = 0 \quad \tilde{r} > 1. \quad (27)$$

For the case of a frictionless contact the traction boundary conditions (16) become

$$\tilde{\sigma}_{31} + \tilde{\tau}_{31} = \tilde{\sigma}_{32} + \tilde{\tau}_{32} = \tilde{m}_{33} = \tilde{m}_{31} = \tilde{m}_{32} = 0 \quad \text{on} \quad \tilde{x}_3 = 0 \quad \text{and} \quad \tilde{r} \leq 1 \quad (28)$$

and for a sticking punch the displacement constraints (17) transform to

$$\tilde{u}_1 = \tilde{u}_2 = \tilde{\omega}_1 = \tilde{\omega}_2 = \tilde{\omega}_3 = 0. \quad (29)$$

It can be seen that the above transformation of variables maps the moving boundary problem of an increasing contact size with increasing indentation depth into a fixed boundary-value problem of unit contact radius. Moreover, a , h and D enter only in the combination c^m as defined in eqn (26). The eigenvalue c^m is determined by solving the reduced problem defined by eqns (23)–(29) such that the normal traction σ_{33} at the edge of the contact vanishes: this is demanded by the requirement that the edge of the contact be

smooth. The eigenvalue c^m is a function of the hardening index n , indenter shape index m and the ratio $\tilde{\ell}$ of the material length scale ℓ to the indentation radius a . In the limit $\ell \rightarrow 0$ the strain gradient theory simplifies to conventional von Mises deformation theory and c^m becomes an invariant of the indentation process itself, i.e. it is independent of a , h and D .

The load P applied to the indenter is

$$P = -2\pi \int_0^a [\sigma_{33}(r)r] dr \quad (30)$$

where σ_{33} is evaluated on the surface $x_3 = 0$. The indentation hardness H is defined as the average pressure on the indenter, and is given by

$$H \equiv \frac{P}{\pi a^2} = -\sigma_0 \left[\left(\frac{a}{D} \right)^{m-1} \frac{1}{\varepsilon_0} \right]^{1/n} \int_0^1 \bar{\sigma}_{33}(\bar{r}) 2\bar{r} d\bar{r} \quad (31)$$

in terms of the reduced variables. Hence, the hardness can be expressed in the functional form

$$H = \sigma_0 \left[\left(\frac{a}{D} \right)^{m-1} \frac{1}{\varepsilon_0} \right]^{1/n} F_a(n, m, \tilde{\ell}) \quad (32)$$

where F_a is a non-dimensional factor which, for a strain gradient theory solid, depends on the hardening index n , the indenter geometrical parameter m , and on the micro length scale $\tilde{\ell}$. For a conical indenter m equals unity and $(a/D)^{m-1}$ is replaced by $\cot \beta$, where 2β is the including cone angle; for a flat indenter $m = \infty$ and $(a/D)^{m-1}$ is replaced by h/a . It is emphasized that the dependence of F_a on $\tilde{\ell}$ reflects the *size dependence* of hardness.

4. FINITE ELEMENT IMPLEMENTATION

4.1. Kinematics

It is convenient to express the field quantities in terms of the circular cylindrical coordinate system (r, z, θ) as shown in Fig. 1. Both the geometry and loading are axisymmetric, and without loss of generality we consider the section $\theta = 0$. The indented solid is subjected to the displacement field

$$u_r = u_r(r, z) \quad u_\theta \equiv 0 \quad u_z = u_z(r, z) \quad (33)$$

and the micro-rotation field

$$\text{and } \omega_\theta = \omega_\theta(r, z) \quad \text{and } \omega_r = \omega_z \equiv 0. \quad (34)$$

The non-vanishing components of the symmetric strain tensor ε are

$$\varepsilon_{rr} = \frac{\partial u_r}{\partial r} \quad \varepsilon_{rz} = \varepsilon_{zr} = \frac{1}{2} \left(\frac{\partial u_r}{\partial z} + \frac{\partial u_z}{\partial r} \right) \quad \varepsilon_{\theta\theta} = \frac{u_r}{r} \quad \text{and} \quad \varepsilon_{zz} = \frac{\partial u_z}{\partial z} \quad (35)$$

and the micro curvature tensor $\chi \equiv \omega \hat{\nabla}$ has the components

$$\chi_{r\theta} = -\frac{\omega_\theta}{r} \quad \chi_{\theta r} = \frac{\partial \omega_\theta}{\partial r} \quad \text{and} \quad \chi_{\theta z} = \frac{\partial \omega_\theta}{\partial z}. \quad (36)$$

The anti-symmetric tensor α has the only non-trivial component

$$\alpha_{zr} \equiv -\alpha_{rz} = \omega_\theta - \frac{1}{2} \frac{\partial u_r}{\partial z} + \frac{1}{2} \frac{\partial u_z}{\partial r}. \quad (37)$$

4.2. Modification of the constitutive law

For the purposes of numerical implementation we modify the original formulation to allow for slight elastic compressibility. Further, the rotation ω is treated as an independent kinematic variable, with no direct dependence upon the displacement \mathbf{u} . The constitutive law (12) is given an additional minor modification such that the initial tangent modulus is finite: the material constants are so chosen that the material response closely matches that of a power law incompressible solid (12) at strain levels in excess of ε_0 .

In the revised formulation, the strain quantities $\boldsymbol{\varepsilon}$ and $\boldsymbol{\chi}$ are split into compressible elastic components which depend linearly upon the stress measures $\boldsymbol{\sigma}$ and \mathbf{m} , and into incompressible plastic components which depend non-linearly upon $(\boldsymbol{\sigma}, \mathbf{m})$. In like fashion, the energy density $w(\boldsymbol{\varepsilon}, \boldsymbol{\chi})$ is written as the sum of an elastic energy density w^e and a plastic energy density w^p . The elastic energy density is defined as

$$w^{el}(\boldsymbol{\varepsilon}^{el}, \boldsymbol{\chi}^{el}) = \int_0^{\boldsymbol{\varepsilon}^{el}} \boldsymbol{\sigma}_{ij} d\boldsymbol{\varepsilon}_{ij}^{el} + \int_0^{\boldsymbol{\chi}^{el}} m_{ji} d\boldsymbol{\chi}_{ij}^{el} \quad (38)$$

where the elastic strains $(\boldsymbol{\varepsilon}^{el}, \boldsymbol{\chi}^{el})$ are linear in the stresses (σ_{ij}, m_{ij}) according to

$$\varepsilon_{ij}^{el} = \frac{1+\nu}{E} s_{ij} + \frac{1-2\nu}{3E} \sigma_{kk} \delta_{ij} \quad \ell \chi_{ji}^{el} = \frac{1+\nu}{E} \ell^{-1} m_{ij}. \quad (39)$$

Here, δ_{ij} is the usual Kronecker symbol, $s_{ij} = \sigma_{ij} - \delta_{ij} \sigma_{kk}/3$ is the deviatoric stress measure, ν is Poisson's ratio and E is Young's modulus. The length scale ℓ is the characteristic micro length scale of the material. The incompressible limit is approached numerically by adopting a value for ν of 0.49999.

The plastic strain energy density w^{pl} is defined as

$$w^{pl}(\boldsymbol{\varepsilon}^{pl}, \boldsymbol{\chi}^{pl}) = \int_0^{\boldsymbol{\varepsilon}^{pl}} \boldsymbol{\sigma}_{ij} d\boldsymbol{\varepsilon}_{ij}^{pl} + \int_0^{\boldsymbol{\chi}^{pl}} m_{ji} d\boldsymbol{\chi}_{ij}^{pl} \quad (40)$$

and, following Fleck *et al.* (1994), w^{pl} is taken to depend only on the overall equivalent plastic strain measure of $\mathcal{E}^{pl} \equiv \sqrt{(\varepsilon_e^{pl})^2 + \ell^2 (\chi_c^{pl})^2}$, where $\varepsilon_e^{pl} \equiv \sqrt{2\varepsilon_{ij}^{pl} \varepsilon_{ij}^{pl}/3}$ is the equivalent plastic strain and $\chi_c^{pl} \equiv \sqrt{2\chi_{ij}^{pl} \chi_{ij}^{pl}/3}$ is the equivalent plastic curvature. The work conjugate of \mathcal{E}^{pl} is the overall equivalent stress Σ as defined in eqn (11). The incompressible plastic strain $(\boldsymbol{\varepsilon}_{ij}^{pl}, \boldsymbol{\chi}_{ij}^{pl})$ is given by

$$\varepsilon_{ij}^{pl} = \frac{3}{2} \left(\frac{1}{E_s(\Sigma)} - \frac{1}{E} \right) s_{ij} \quad \ell \chi_{ji}^{pl} = \frac{3}{2} \left(\frac{1}{E_s(\Sigma)} - \frac{1}{E} \right) \ell^{-1} m_{ij} \quad (41)$$

where E_s is the secant modulus in uniaxial tension and E is Young's modulus. The above elastic relations (39) and plastic relations (41) can be combined to give

$$e_{ij} = \frac{1+\nu_s}{E_s} s_{ij} \quad \ell \chi_{ji} = \frac{1+\nu_s}{E_s} \ell^{-1} m_{ij} \quad \text{and} \quad \varepsilon_{kk} = \frac{1-2\nu}{3E} \sigma_{kk} \quad (42)$$

where the deviatoric strain $e_{ij} = \varepsilon_{ij} - \delta_{ij} \varepsilon_{kk}/3$ and $\nu_s = 1/2 - (1/2 - \nu)E_s/E$. The overall equivalent strain is given by $\mathcal{E} = \Sigma/E + \mathcal{E}^{pl}$.

The power-law constitutive law (12) suffers from the drawback that the initial tangent modulus is unbounded. A finite tangent stiffness is needed in order to construct a non-singular stiffness matrix in the finite element formulation detailed below. Accordingly, the

power law relation (12) is modified to the following form which possesses a finite initial tangent modulus :

$$\frac{\mathcal{E}}{\varepsilon_0} = \frac{\arcsin(\Sigma \sin \phi / \sigma_0)}{\phi} \quad \text{for } \Sigma < \sigma_0 \quad (43)$$

and

$$\frac{\mathcal{E}}{\varepsilon_0} = \left(\frac{\Sigma}{\sigma_0} \right)^n \quad \text{for } \Sigma \geq \sigma_0. \quad (44)$$

Here, the magnitude of the parameter ϕ is chosen to satisfy

$$\frac{\tan \phi}{\phi} = n \quad (45)$$

which ensures continuity of both value and slope of the Σ vs \mathcal{E} curve at $\Sigma = \sigma_0$. Only the smallest positive root of eqn (45) is chosen for any given value of strain hardening exponent n ; it can be seen that ϕ increases from zero to $\pi/2$ as n is increased from unity to infinity. The modification (43)–(45) to (12) gives a Σ vs \mathcal{E} curve of finite initial slope

$$E = \frac{\sigma_0}{\varepsilon_0} \frac{\phi}{\sin \phi}. \quad (46)$$

A preliminary convergence study suggests that the choice $\varepsilon_0 = 10^{-4}h/a$ (with $h/a = 0.01$) is sufficiently small for the constitutive law (33) and (34) to give the same indentation response as the power law constitutive law (12). (Upon reducing ε_0 from 10^{-4} to 10^{-5} , it was found that the indentation pressure changed by less than 0.1% for any n .)

In a related indentation study Bower *et al.* (1993) employed the following approximation to power-law hardening :

$$\frac{\varepsilon}{\varepsilon_0} = \frac{n}{n-1} - \left[\frac{1+n^2}{(n-1)^2} - \left(\frac{\sigma}{\sigma_0} + \frac{1}{n-1} \right)^2 \right]^{1/2} \quad \text{for } \sigma < \sigma_0 \quad (47)$$

and

$$\frac{\varepsilon}{\varepsilon_0} = \left(\frac{\sigma}{\sigma_n} \right)^n \quad \text{for } \sigma \geq \sigma_0. \quad (48)$$

This gives a Young's modulus of $E = n\sigma/\sigma_0$; consequently, E is large at large n and this leads to poor convergence of the numerical procedure. Convergence difficulties were reported by Bower *et al.* (1993) for $n > 5$ and a displacement relaxation method, in addition to parameter tracking, was used to obtain solutions at large values of n . By adopting the modified constitutive law (43)–(45), coupled with parameter tracking only, we were able to obtain converged solutions for any value of n . The parameter-tracking method is similar to that described by Shih and Needleman (1984) and Bower *et al.* (1993), and consists of obtaining a solution for successively higher values of n by taking the solution from the previous value of n as the initial guess.

In order to implement the Fleck and Hutchinson (1993) strain gradient theory within the framework of the finite element method, special care has to be taken with regard to the curvature χ_{ij} . The Fleck and Hutchinson theory falls within the class of reduced couple stress theory wherein χ_{ij} is expressed in terms of the second derivative of the displacement field; this suggests the use of elements of C_1 -continuity. Here, we enforce the kinematic constraint $\omega = \theta \equiv (1/2)\text{curl} \mathbf{u}$ by a penalty function method and treat the rotation ω as an independent degree of freedom; consequently, we can use elements of C_0 -continuity. The

anti-symmetric shear stress τ_{ij} is assumed to be related to α_{ji} through a constant penalty modulus G_a as

$$\tau_{ij} = G_a \alpha_{ji} \quad (49)$$

and the identify $\omega = \theta \equiv (1/2)\text{curl}\mathbf{u}$ is approached numerically by choosing a sufficiently large value of G_a . Numerical experiments show that accurate results are obtained by taking $G_a = 100E$.

A modified Newton–Raphson method is used to solve the non-linear boundary value problem outlined in Section 3. Briefly, the indenter displacement h is incremented from zero to $h = 0.01a$ at fixed a , and the nodal displacements (\mathbf{u}, ω) are calculated for each load step by expanding the principle of virtual work about the current solution, giving

$$\begin{aligned} & \int_V (\Delta s_{ij} \delta e_{ij} + \Delta m_{ij} \delta \chi_{ji} + \Delta \sigma_m \delta \varepsilon_{kk} + \Delta \tau_{ij} \delta \alpha_{ji}) dv - \int_S (\Delta T_j \delta u_j + \Delta Q_j \delta \omega_j) ds \\ & = - \left\{ \int_V (s_{ij} \delta e_{ij} + m_{ij} \delta \chi_{ji} + \sigma_m \delta \varepsilon_{kk} + \tau_{ij} \delta \alpha_{ji}) dv - \int_S (T_j \delta u_j + Q_j \delta \omega_j) ds \right\} \quad (50) \end{aligned}$$

where $\sigma_m = \sigma_{kk}/3$ is the mean stress. Stresses and couple stresses on the right-hand side of eqn (50) denote the current approximate solution and Δ indicates the correction for the current iteration. The virtual work statement (50) is solved repeatedly for displacement corrections until a converged solution is obtained. In order to minimize computational time, the tangent stiffness matrix is calculated at the beginning of each load step and held fixed during iteration. The tangent stiffness matrix is calculated from the following rate form of the constitutive law :

$$\dot{s}_{ij} = \frac{E}{1 + \nu_s} [\dot{e}_{ij} + \lambda s_{ij} (s_{kl} \dot{e}_{kl} + m_{kl} \dot{\chi}_{lk}) / \Sigma^2] \quad (51)$$

and

$$\ell^{-1} \dot{m}_{ij} = \frac{E_s}{1 + \nu_s} [\ell \dot{\chi}_{ij} + \lambda \ell^{-1} m_{ij} (s_{kl} \dot{e}_{kl} + m_{kl} \dot{\chi}_{lk}) / \Sigma^2] \quad (52)$$

where

$$\lambda = \frac{9 E_s \Sigma}{4 E_s} \frac{1}{1 + \nu_s - E_s \Sigma / (2 E_s)} \quad (53)$$

and $E'_s = dE_s/d\Sigma$. In addition,

$$\dot{\sigma}_m = \frac{E}{3(1 - 2\nu)} \dot{\varepsilon}_{kk} \quad \text{and} \quad \dot{\tau}_{ij} = G_a \dot{\alpha}_{ji}. \quad (54)$$

4.3. Type of elements and the integration scheme

We have implemented the strain gradient theory within a finite element procedure, with two types of axisymmetric isoparametric elements : the 9-noded quadrilateral and 6-noded triangle. Three degrees-of-freedom u_r , u_z and ω_θ exist at each node, as shown in Fig.

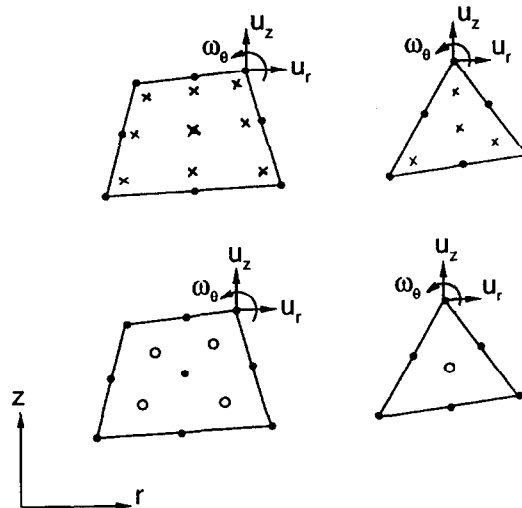


Fig. 2. C_0 isoparametric elements developed for the strain gradient theory solid: (i) 9-noded quadrilateral; and (ii) 6-noded triangular elements. For both types of element: \bullet denotes a node; \times indicates an integration point for the deviatoric stresses and couple stress; and \circ represents an integration point for the mean stress and the anti-symmetric shear stress.

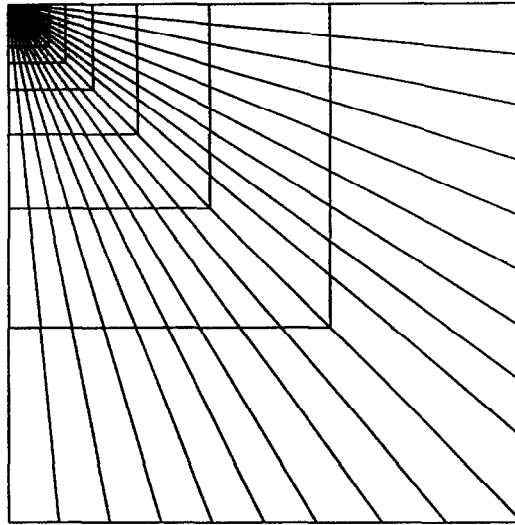
2, and quadratic shape functions are used for interpolation between nodes [see Zienkiewicz and Taylor (1994)]. In the principle of virtual work (40), full integration is used for the deviatoric terms: 3×3 Gauss quadrature for the 9-noded elements and four point Gauss–Radau quadrature for the 6-noded elements. Since the elastic bulk modulus $K \equiv E/(1-2\nu)$ and the anti-symmetric shear modulus G_a are significantly greater than Young’s modulus E , reduced integration is used for the mean stress and the anti-symmetric shear stress to avoid locking of the elements. Specifically, 2×2 point Gaussian quadrature is used for the 9-noded elements and 1-point Gauss–Radau quadrature is employed for the 6-noded elements. Numerical experimentation indicates that the 9-noded element passes the single element test and the patch test, and gives smooth distributions of hydrostatic stress and anti-symmetric shear stress. The 6-noded triangle with one-point reduced integration fails both the single element test and the patch test (it passes both tests for plane strain deformation). However, a ring of these triangular elements at the contact edge are found to be less stiff than triangular elements with three-point reduced integration and give an accurate contact pressure distribution.

Xia and Hutchinson (1996) have conducted an extensive search for the optimal choice of element in their finite element analysis of a mode I crack tip field in a strain gradient theory solid. The C_1 -continuous plate-bending elements formulated by Specht (1988) were found to perform poorly. Xia and Hutchinson also considered C_0 -continuous isoparametric elements, in the form of 4-noded and 9-noded quadrilaterals, and 3-noded and 6-noded triangles. They adopted a mixed formulation, with two displacement and one rotational degree-of-freedom at each node, and the antisymmetric shear stress τ_{rz} acting as a Lagrange multiplier at the centre of each element. Thus, the kinematic constraint $\omega = \theta \equiv (1/2)\text{curl}\mathbf{u}$ is satisfied in an element-wide average sense. In contrast, the incompressibility condition is tackled by a reduced integration penalty method.

In the present study, we prefer to use a formulation purely based on displacement and rotation interpolation, coupled with a reduced integration penalty method; this approach has the merits of simplicity, a relatively small number of degrees-of-freedom and less computational effort. Bench mark tests, as described in detail in the Appendix, show that the C_0 elements are adequate.

The similarity transform, outlined in Section 3, allows for the reduction of the moving contact problem of indentation by a curved indenter to that of indentation over a fixed contact radius a . All calculations were performed for a contact of unit radius, using the mesh shown in Fig. 3. The mesh consists of 2239 elements and 9013 nodes and has a total of 27,039 degrees-of-freedom. Except for 40 triangular elements adjoining the contact edge,

(a)



(b)

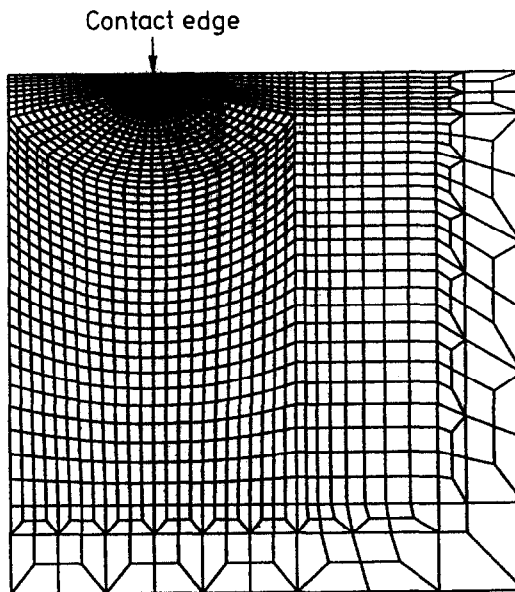


Fig. 3. Typical finite element mesh used, with 2239 elements and 9013 nodes: (a) full mesh; and (b) mesh close to the contact.

all other elements are 9-noded quadrilateral. The boundaries of the mesh form a square of dimension 100 times the contact radius, and is subjected to the boundary conditions (14)–(17). Additional boundary conditions are:

- (i) along the axisymmetric axis, $u_r = \omega_\theta = 0$ and $\sigma_{rz} + \tau_{rz} = 0$;
- (ii) along the bottom edge of the mesh $u_z = \omega_\theta = 0$ and $\sigma_{zr} + \tau_{zr} = 0$;
- (iii) the side of the mesh is traction-free.

In order to solve the problem of indentation of a half-space by a curved indenter of power-law head-shape the following procedure is adopted. First, the solution is obtained for indentation by a flat punch of unit radius $a = 1$ subjected to a uniform displacement $u_z = -h$ for some arbitrary value of h . Second, the surface displacement field associated

with the flat-punch solution is relaxed by an amount $u_z = r^m/D^{m-1}$ over the fixed contact ($r \leq a = 1$); the indenter size D is adjusted by iteration until the contact pressure at the perimeter vanishes. An initial value for D specified by $1/D^{m-1} = 0.1h$ is used in the computation. Substitution of the converged value for D into eqn (26) gives the eigenvalue c^m . For a conical indenter, $m = 1$ and D^{m-1} can be interpreted as $\cot \beta$ where 2β is the angle of the cone. In order to evaluate the contact pressure accurately at the edge of the mesh a refined mesh is employed (see Fig. 3).

5. RESULTS AND DISCUSSION

5.1. Effect of indent size upon hardness

The effect of indenter size a on the predicted hardness H is shown in Fig. 4 for three head-shapes (flat punch, cone and ball) and for n in the range of 1–5. The values of H for the strain gradient solid have been normalized by the indentation hardness for the conventional solid ($\ell = 0$), as summarized in Table 1.

Consider first the case of a frictionless indenter, Fig. 4(a). For all head-shapes and strain hardening exponents considered there is a continuous increase in hardness with diminishing indenter size. With increasing n , both the size effect and the effect of head-shape on hardness diminish: the size effect is most pronounced for indentation of a linear solid by a spherical indenter such that the hardness nearly doubles when the indenter size a is reduced from $a \gg \ell$ to $a = \ell$. In contrast, for the case of ball indentation and $n = 5$, the hardness increases by only 10% when a is reduced from $a \gg \ell$ to $a = \ell$. This predicted size effect is significantly less than that observed experimentally. For example, Poole *et al.* (1995) found that the hardness of copper ($n \approx 5$) almost doubles when the indentation depth of a Vickers indenter is reduced from a large value to $a \approx 1 \mu\text{m}$. It is known from the torsion tests of Fleck *et al.* (1994) that the material length scale for copper is on the order of $\ell \approx 2 \mu\text{m}$. It is thought that the Fleck–Hutchinson strain gradient theory underpredicts the indentation size effect largely because the theory neglects the effect of stretch gradients. In the more general theory of Fleck and Hutchinson (1997) the role of stretch gradients is included. Recently, Begley and Hutchinson (1996) have included the additional strengthening due to stretch gradients and they report a size effect in agreement with the experimental data of Poole *et al.* (1995). Xia and Hutchinson (1996) reached a similar conclusion in their analysis of stress elevation by strain gradients ahead of a mode I crack tip. They found that the Fleck–Hutchinson strain gradient theory led to only slightly enhanced stresses ahead of a mode I crack.

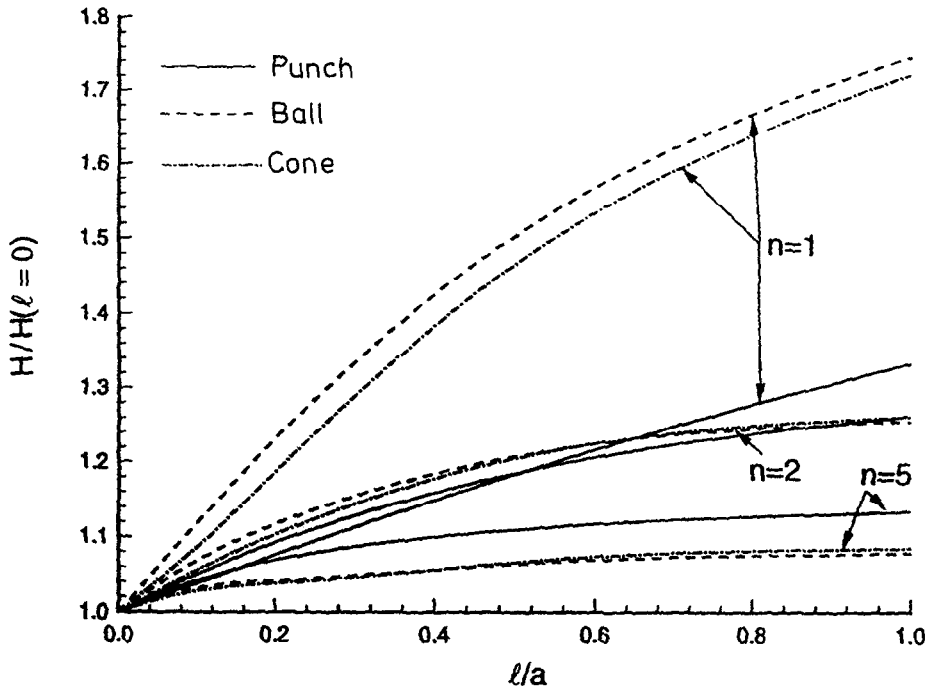
We have also considered the effect of friction on indentation hardness for the case of a flat-ended punch. For the conventional solid the effect of sticking friction is to increase the hardness by about 10% compared to a frictionless punch, for all n values considered (see Table 1). The effect of friction is more marked for the strain gradient solid, particularly at high values of n , as shown in Fig. 4(b). For example, at $\ell/a = 1$ and $n = 5$ the hardness for the sticking punch is more than twice that for the frictionless punch. The enhanced size effect for sticking friction is consistent with the argument that sticking friction leads to a greater degree of shear and rotation of material points adjacent to the indenter.

We have not been able to obtain reliable hardness results for a conical or spherical indenter due the presence of an oscillating contact pressure distribution near the sticking contact edge. Further work is required in order to separate the roles of the friction law and the role of stretch gradients in contributing to the size effect observed for spherical and conical indenters.

5.2. Contact pressure distribution

The distribution of contact pressure beneath a frictionless indenter is shown in Fig. 5(a) for the flat-ended punch, in Fig. 6 for a spherical indenter and in Fig. 7 for a conical indenter. Reliable solutions were also obtained for the case of a sticking flat punch [see Fig. 5(b)]. The oscillation in pressure near the contact edge for the sticking indenter prevented us from obtaining a converged solution with vanishing pressure at the contact perimeter for the sticking conical indenter and sticking spherical indenter.

(a)



(b)

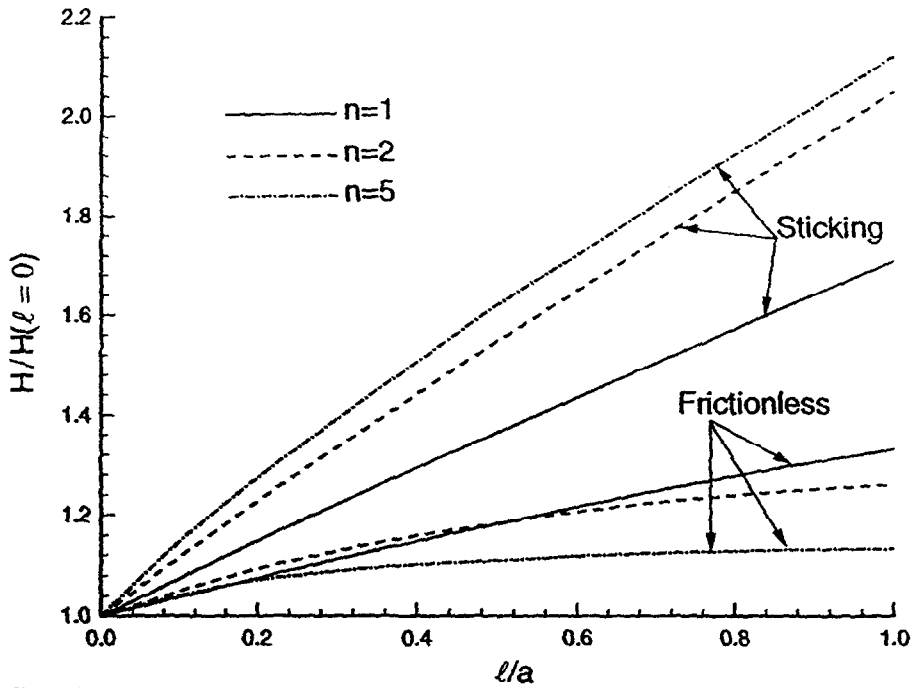


Fig. 4. The normalized hardness $H/H(\ell = 0)$ vs ℓ/a , where a is the radius of the flat-ended indenter: (a) frictionless indenter of various head-shape; (b) flat-ended sticking indenter.

Table 1. $F_a(n, m, \ell/a = 0)$

$1/n$	Frictionless flat punch ($m = \infty$)	Sticking flat punch ($m = \infty$)	Frictionless ball ($m = 2$)	Frictionless cone ($m = 1$)
1.0	0.853	0.853	1.122	0.663
0.9	1.082	1.082	1.198	0.742
0.8	1.336	1.336	1.284	0.835
0.7	1.607	1.608	1.383	0.945
0.6	1.891	1.894	1.449	1.079
0.5	2.180	2.186	1.638	1.241
0.4	2.467	2.477	1.814	1.445
0.3	2.738	2.757	2.027	1.695
0.2	2.969	3.003	2.272	1.990
0.1	3.104	3.174	2.519	2.296

First, consider the results for the frictionless flat punch [Fig. 5(a)]. The boundary conditions at the edge of the punch are identical to those at mode I crack tip, and the asymptotic analyses of Huang *et al.* (1997) and Xia and Hutchinson (1996) can be used directly. These analyses reveal that the pressure p varies with distance s from the indenter edge according to $p \propto s^{-1/(n+1)}$ for both the conventional solid, $\ell = 0$, and for the strain gradient solid, $\ell = a$. For $\ell = 0$ the singularity at the edge of the contact is precisely the mode I HRR singularity; for the strain gradient solid, the field has the curious feature that both the Cauchy stress and the couple stress vary according to $s^{-1/(n+1)}$. This is a consequence of the feature that the most singular permissible strain field is irrotational, as discussed by Xia and Hutchinson (1996). It is clear from Fig. 5(a) that the effect of indenter size ℓ/a upon contact pressure is small. For both $\ell/a = 0$ and $\ell/a = 1$ the contact pressure distribution becomes more uniform with increasing n .

Next, consider the contact pressure for the sticking flat-punch, Fig. 5(b). For clarity of presentation results are shown only for $n = 1$, and $\ell/a = 0$ and 1. It is clear that the stress field is singular at the edge of the punch for both $\ell/a = 0$ and $\ell/a = 1$. For $\ell/a = 0$ the pressure increases monotonically as the contact edge is approached, whereas for $\ell/a = 1$ the pressure distribution oscillates near the contact edge. The oscillatory behaviour is reminiscent of the crack tip field for an interfacial crack between dissimilar elastic solids. A convergence study suggests that the contact pressures displayed in Fig. 5(b) is independent of type and size of the mesh except for a small zone adjacent to the contact edge of width $0.02a$. We believe the total load calculated is reliable although the oscillating pressure is approximate within the narrow region near the contact edge.

Now consider results for the spherical indenter and the conical indenter. The pressure distribution beneath the frictionless spherical indenter is approximately elliptical in shape for n in the range 1–5, and for $\ell/a = 0$ and 1 (see Fig. 6). (Recall the pressure distribution is an ellipse for the Hertz solution, $n = 1$ and $\ell/a = 0$.) There is only a small effect of length scale ℓ/a upon the pressure distribution: the pressure at the edge of the contact increases somewhat with increasing ℓ/a . The conical indenter induces a singular stress distribution at the apex of the indenter (see Fig. 7). The nature of this singularity has been explored previously for the conventional solid by Durban and Fleck (1991). In broad terms the stress field at the tip of a frictionless cone has a power law dependence upon radial distance from the apex, but is less singular than the HRR crack singularity. It is clear from Fig. 7 that the pressure distribution becomes more uniform over the contact with increasing n ; the effect of length scale ℓ/a upon the pressure distribution is minor.

The nature of the indentation field is illustrated by plotting contours of overall effective strain $\tilde{\mathcal{E}}_e$ beneath the indenter. Contour plots are given for the frictionless punch in Fig. 8(a), the sticking flat punch in Fig. 8(b), the frictionless ball in Fig. 9(a) and for the frictionless cone in Fig. 9(b). The solid lines of Fig. 8(a) are contours of normalized equivalent strain $\tilde{\mathcal{E}}_e$ under a frictionless flat-ended indenter, for $\ell = a$ and $n = 5$. The distribution of the normalized von Mises strain $\tilde{\varepsilon}_e$ is only marginally different from that of $\tilde{\mathcal{E}}_e$ and are not included in the figure. Note that the contours of $\tilde{\mathcal{E}}_e$ are almost semi-circular near the contact edge; this is in agreement with the analytical solution for the mode I crack

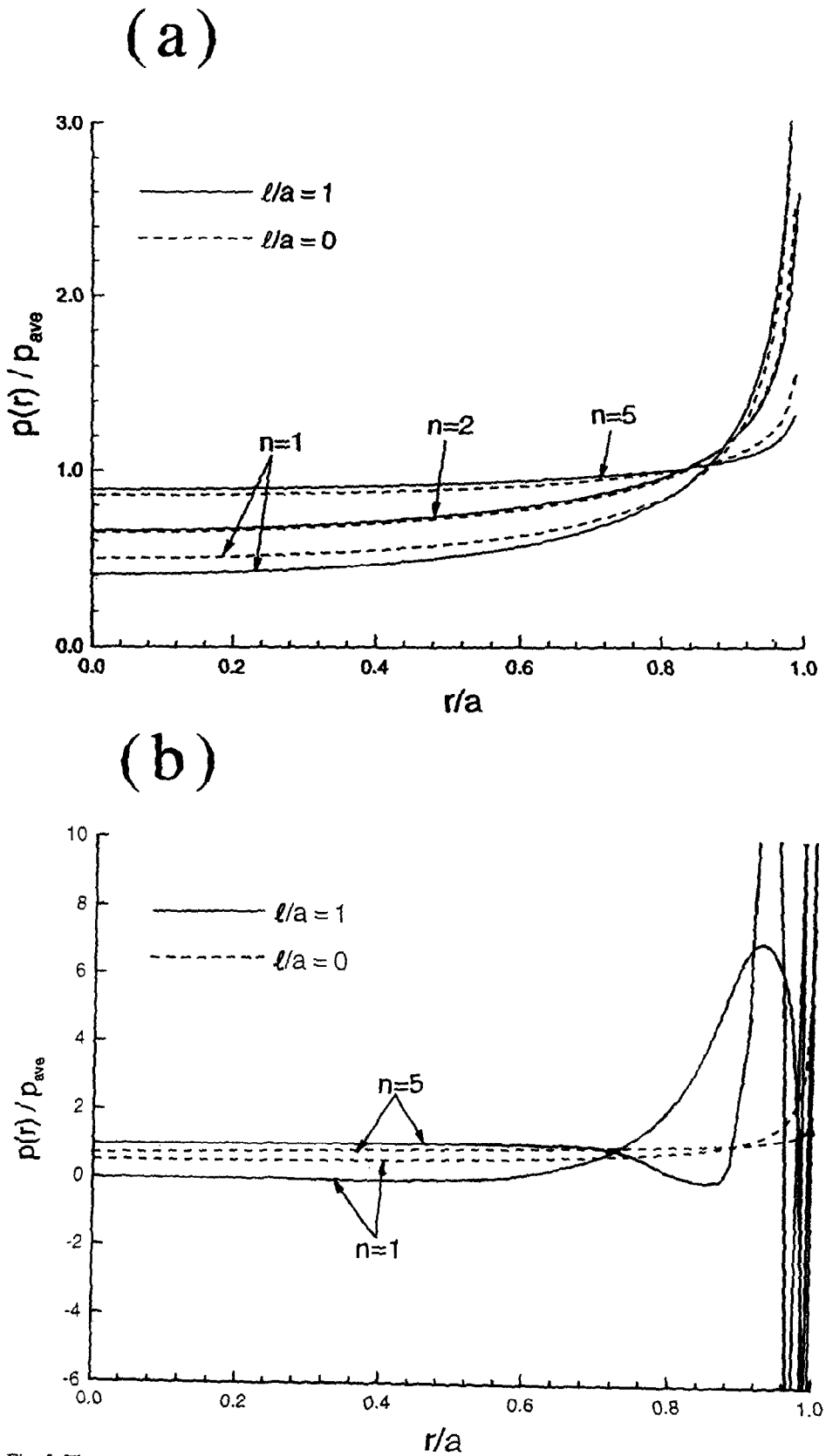


Fig. 5. The pressure distribution under a flat-ended indenter: (a) frictionless contact; (b) sticking contact. $l/a = 0$ and 1, and $n = 1, 2$ and 5.

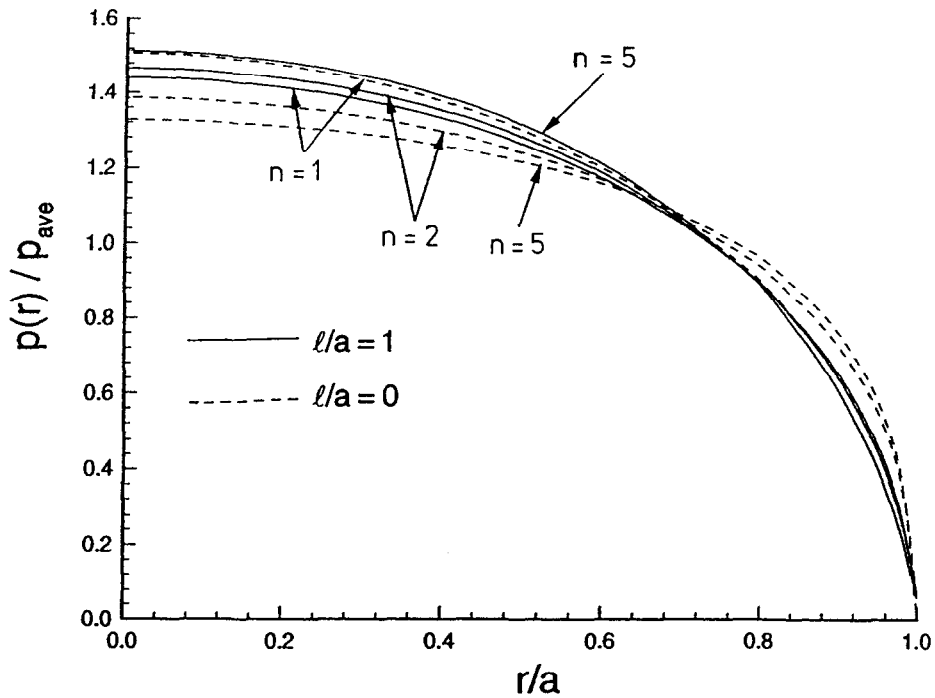


Fig. 6. The contact pressure distribution under a frictionless spherical indenter, for $l/a = 0$ and 1, and $n = 1, 2$ and 5.

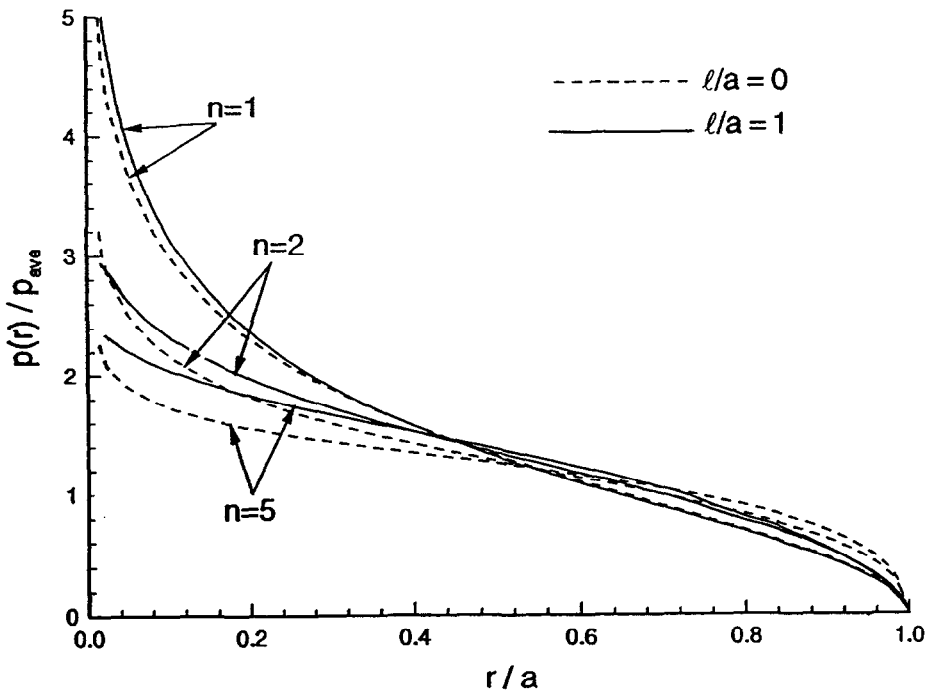


Fig. 7. The contact pressure distribution under a frictionless conical indenter, for $l/a = 0$ and 1, and $n = 1, 2$ and 5.

tip field in the strain gradient solid presented by Xia and Hutchinson (1996) and by Huang *et al.* (1997). For the conventional solid ($l/a = 0$ and $\tilde{\mathcal{E}}_e = \tilde{\varepsilon}_e$) there is a pronounced dependence of $\tilde{\mathcal{E}}_e$ upon angular co-ordinate in the mode I HRR crack tip field. Contours of $\tilde{\mathcal{E}}_e$ for the conventional solid are included in Fig. 8(a) as dashed lines, and display the expected strong dependence upon angular co-ordinate at the edge of the contact.

Contours of $\tilde{\mathcal{E}}_e$ for indentation by a flat-ended sticking punch are shown as solid lines in Fig. 8(b), for $l/a = 1$ and $n = 5$. Contrary to the case of frictionless contact, the contours

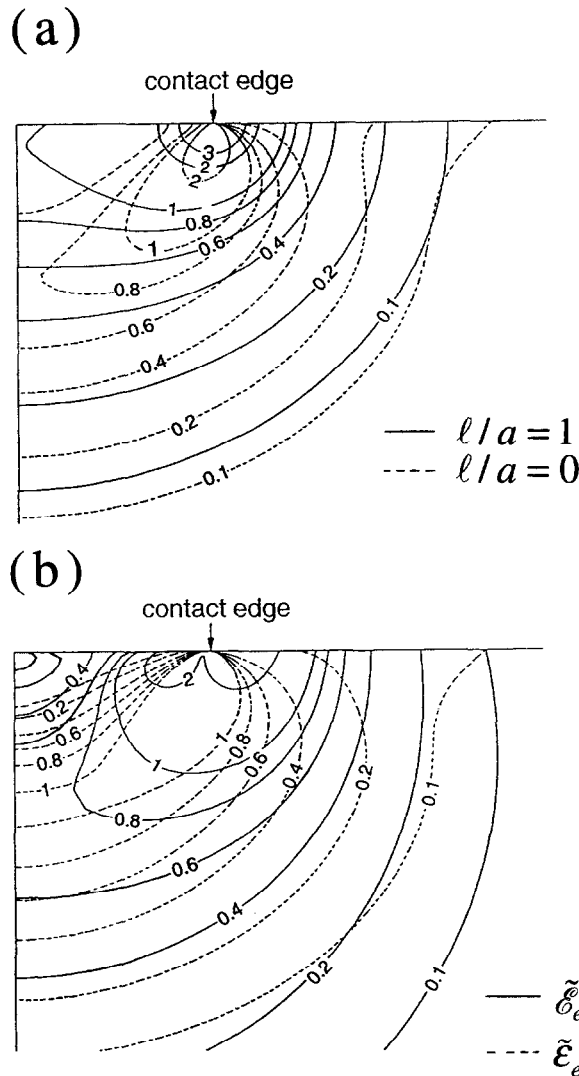


Fig. 8. (a) Contours of normalized equivalent strain $\tilde{\epsilon}_e$ for indentation by a frictionless flat-ended indenter, with $\ell/a = 1$ (solid lines) and $\ell/a = 0$ (dashed lines), and $n = 5$. (b) Contours of normalized equivalent strain $\tilde{\epsilon}_e$ (solid lines) and von Mises strain $\tilde{\epsilon}_m$ (dashed lines) for indentation by a sticking flat-ended indenter, with $\ell/a = 1$ and $n = 5$.

of von Mises equivalent strain $\tilde{\epsilon}_m$ under a sticking punch differ considerably from those of $\tilde{\epsilon}_e$ and are shown in Fig. 8(b) as dashed lines. Maxima in $\tilde{\epsilon}_e$ and $\tilde{\epsilon}_m$ occur at the edge of the contact.

Now consider the distribution of normalized equivalent strain $\tilde{\epsilon}_e$ beneath the frictionless spherical indenter, Fig. 9(a), and beneath the frictionless cone, Fig. 9(b). For both geometries, contour plots are given for $\ell/a = 0$ and 1, and $n = 5$. In all cases the maximum value of $\tilde{\epsilon}_e$ occurs along the centre line. With increasing ℓ/a the distribution of $\tilde{\epsilon}_e$ becomes more diffuse beneath the contact.

5.3. Surface displacement field

The eigenvalue c relates the true contact radius a to the indentation depth h . As discussed by Hill *et al.* (1989) and Bower *et al.* (1993), c has two physical interpretations: (i) it equals the ratio of true contact radius to nominal contact radius, and (ii) it specifies the vertical displacement of the indented half-space at the edge of contact ($\tilde{r} = 1$), see eqn (36). A value $c > 1$ implies pile-up at the contact edge. Recall that for a conventional elastic-plastic solid, c depends on the magnitude of the strain hardening exponent n , indenter shape, and on the contact friction condition. For a strain-gradient elastic-plastic solid the magnitude of c also depends on the ratio of contact radius a to material length

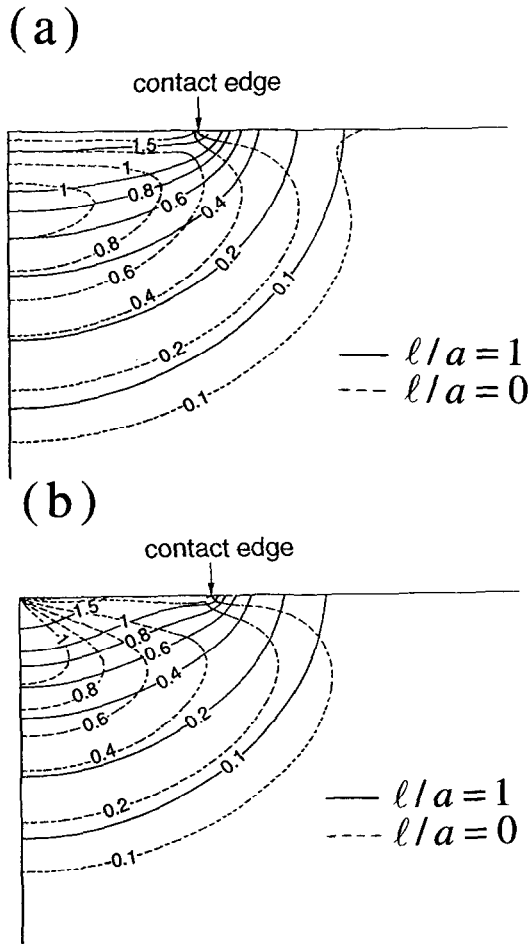


Fig. 9. Contours of normalized equivalent strain $\tilde{\epsilon}_e$ for indentation by (a) frictionless ball; and (b) frictionless cone. In both figures $n = 5$, dashed lines denote $l/a = 0$ and solid lines denote $l/a = 1$.

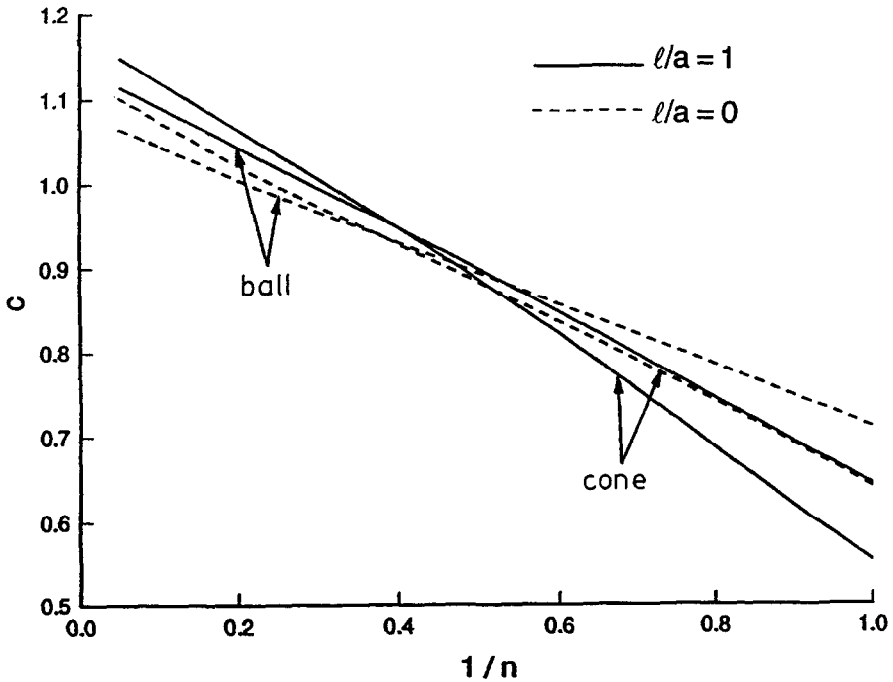


Fig. 10. The eigenvalue c for indentation by frictionless cone ($m = 1$) and frictionless sphere ($m = 2$).

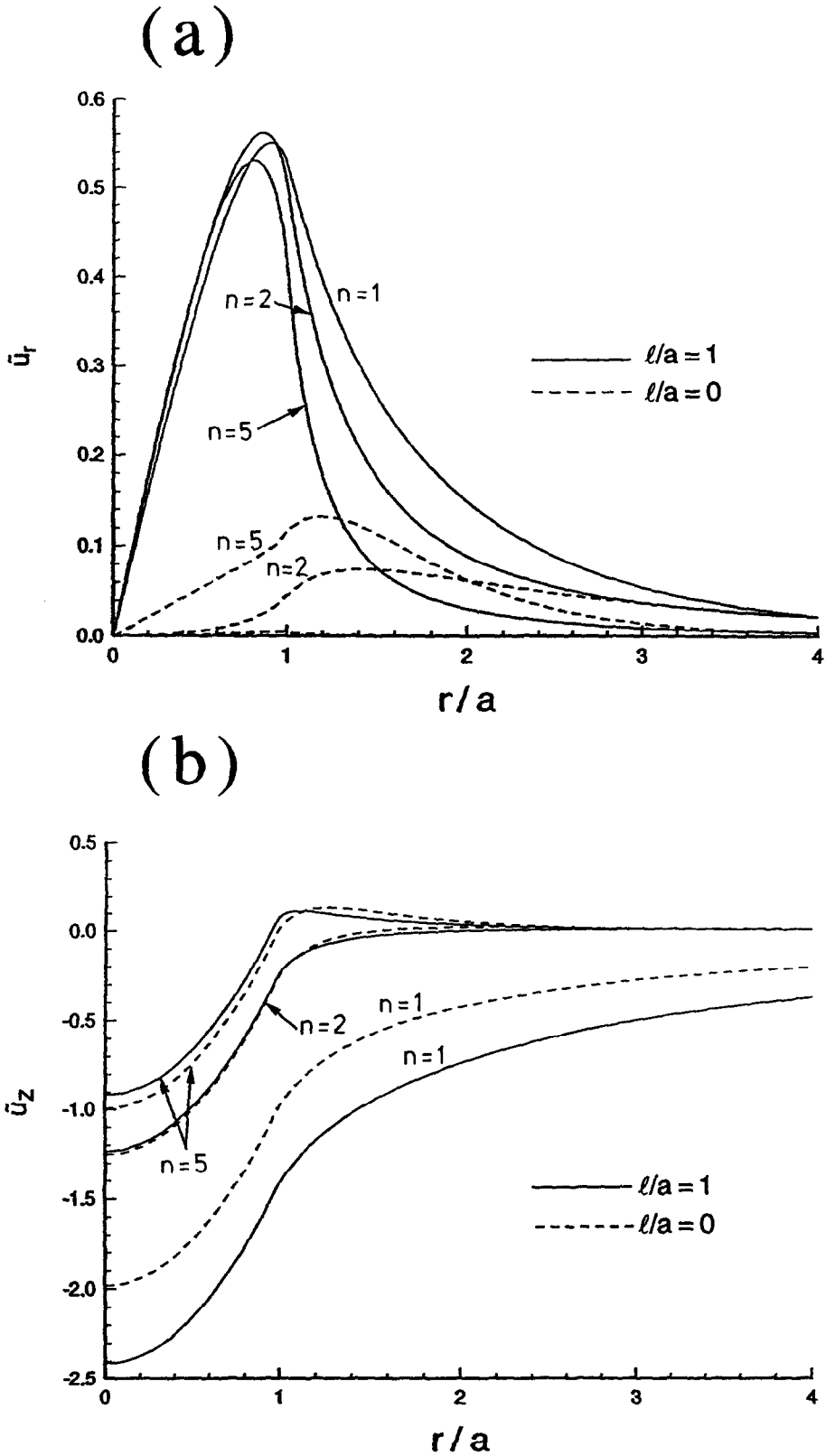


Fig. 11. The normalized surface displacement due to indentation by a frictionless spherical indenter : (a) radial displacement \bar{u}_r ; and (b) vertical displacement \bar{u}_z . $n = 5$, $l/a = 0$ and 1.

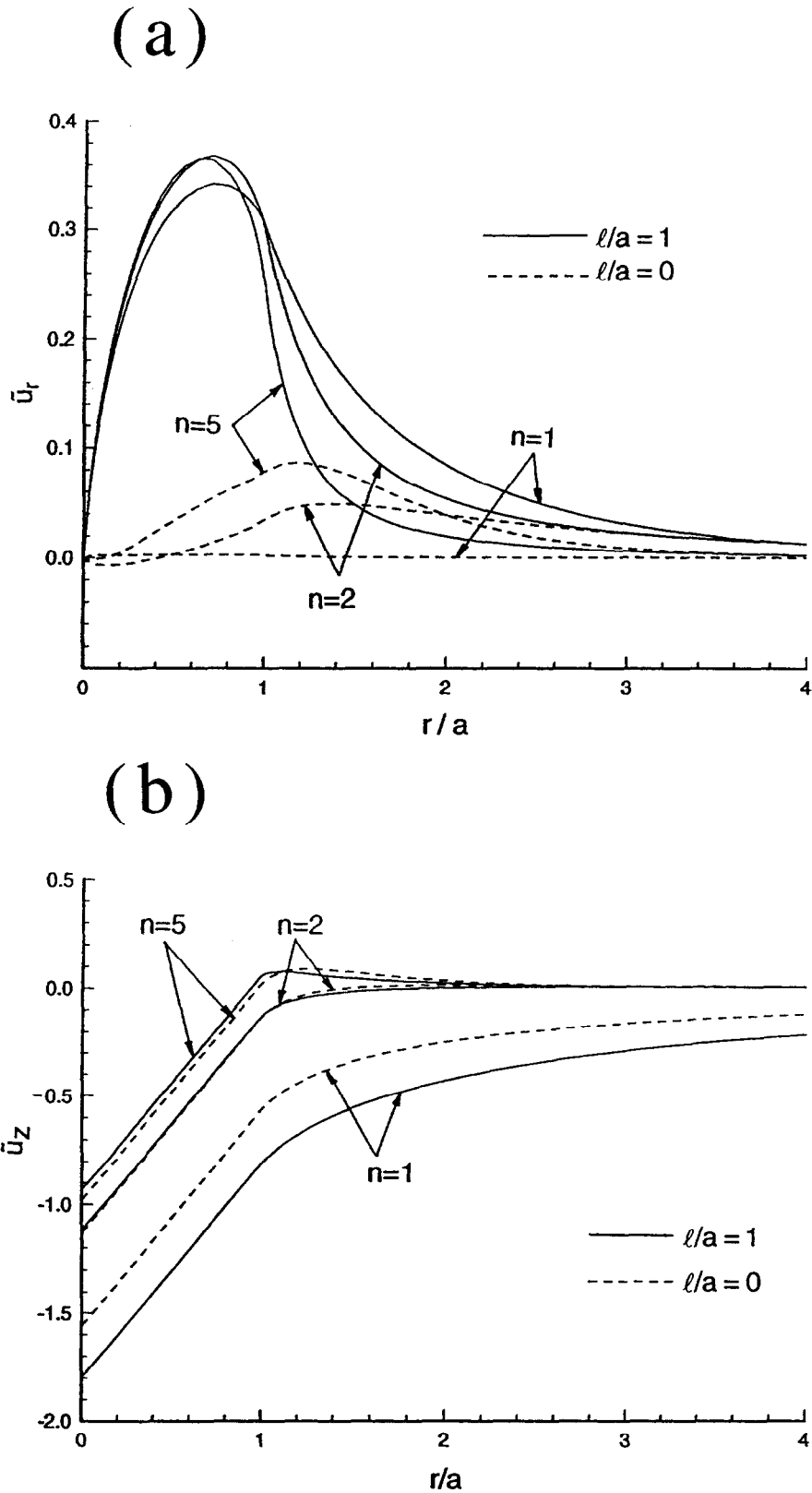


Fig. 12. The normalized surface displacement due to indentation by a frictionless conical indenter: (a) radial displacement \bar{u}_r ; and (b) vertical displacement \bar{u}_z . $n = 5$, $l/a = 0$ and 1.

scale ℓ . Values for c are presented in Fig. 10 for the frictionless ball and cone: there is only a minor effect of length scale ℓ/a upon c . We note in passing that the values calculated for c for $\tilde{\ell} = 0$ agree with those given by Hill *et al.* (1989) to within 1% for all n .

The normalized displacement on the surface $x_3 = 0$ is shown in Fig. 11 for a frictionless spherical indenter and Fig. 12 for a frictionless conical indenter. The physical displacement field for a particular ball diameter or cone angle and a particular indentation depth can be deduced via the scaling relation (19). It can be seen that material piles up at the contact edge at large n , for both the strain gradient solid ($\ell/a = 1$) and for the conventional solid ($\ell/a = 0$). With increasing ℓ/a there is a minor effect upon \tilde{u}_z , but a major increase in \tilde{u}_r is observed for both geometries. The accuracy of these predictions await experimental support.

Acknowledgements—J. Shu acknowledges the financial support from the U.S. Department of Energy through the Lawrence Livermore National Laboratory under contact no. W-7405-Eng-48. N. Fleck acknowledges support from ONR grant N00014-91-J-1916. Both authors wish to thank Dr W. E. King, Dr D. Sam and Professor J. W. Hutchinson for their encouragement and helpful discussions.

REFERENCES

- Begley, M. and Hutchinson, J. W. (1996) Private communication.
- Bower, A. F., Fleck, N. A., Needleman, A. and Ogbonna, N. (1993) Indentation of a power law creeping solid. *Proceedings of the Royal Society of London A* **441**, 97–124.
- Cosserat, E. and Cosserat, F. (1909) *Theorie des Corps Deformables*. Herman, Paris.
- Durban, D. and Fleck, N. A. (1991) Steady penetration of a rigid cone with a rough wall into a power law viscous solid. *Journal of Applied Mechanics* **58**, 872–880.
- Ebeling, R. and Ashby, M. F. (1966) *Philosophical Magazine* **13**, 805.
- Fleck, N. A. and Hutchinson, J. W. (1993) A phenomenological theory for strain gradient effects in plasticity. *Journal of Mechanics and Physics of Solids* **41**, 1825–1857.
- Fleck, N. A. and Hutchinson, J. W. (1997) Strain gradient plasticity. *Advances in Applied Mechanics*, ed. J. W. Hutchinson and T. Y. Wu, **33**, 295–361.
- Fleck, N. A., Muller, G. M., Ashby, M. F. and Hutchinson, J. W. (1994) Strain gradient plasticity: theory and experiment. *Acta Metallurgica et Materiala* **42**(2), 475–487.
- Hill, R., Storakers, B. and Zdunek, A. B. (1989) A theoretical study of the Brinell hardness test. *Proceedings of the Royal Society of London A* **423**, 301–330.
- Huang, Y., Zhang, L., Guo, T. F. and Hwang, K.-C. (1997) Mixed mode near-tip fields for cracks in materials with strain-gradient effects. *Journal of Mechanics and Physics of Solids* **45**, 439–465.
- Johnson, K. L. (1985) *Contact Mechanics*. Cambridge University Press, Cambridge.
- Kelly, A. and Nicholson, R. B. (1963) *Progress in Materials Science* **10**, 151.
- Ma, Q. and Clarke, D. R. (1994) Size dependent hardness of silver single crystals. *Journal of Material Research* **10**(4), 853–863.
- Poole, W. J., Ashby, M. F. and Fleck, N. A. (1996) Micro-hardness tests on annealed and work-hardened copper polycrystals. *Scripta Metallica et Materiala* **34**(4), 559–564.
- Shih, C. F. and Needleman, A. (1984) Fully plastic crack problems. *Journal of Applied Mechanics* **51**, Part I, 48–56.
- Specht, B. (1988) Modified shape functions for the three node plate bending element passing the patch test. *International Journal of Numerical Methods in Engineering* **26**, 705–715.
- Xia, Z. C. and Hutchinson, J. W. (1996) Crack tip fields in strain gradient plasticity. *Journal of Mechanics and Physics of Solids* **44**, 1621–1648.
- Zienkiewicz, O. C. and Taylor, R. L. (1994) *The Finite Element Method*, 4th edn. McGraw-Hill, New York.

APPENDIX

The accuracy of the 9-noded quadrilateral elements and the 6-noded triangular elements was evaluated by comparing against existing results taken from the literature for the limiting case of the conventional solid, ($\tilde{\ell} = 0$). For indentation of a non-linear half-space by a frictionless flat-ended punch, F_a differs by less than 0.2% from the values given by Bower *et al.* (1993) for all values of n . The eigenvalue c^2 for a frictionless ball was also compared with values obtained by Hill *et al.* (1989). For a linear elastic solid, the Hertz's analytical solution is $c^2 = 0.5$, Hill *et al.*'s value is 0.508, while we obtained a value of 0.505. The greatest difference between our results and Hill *et al.*'s results is about 0.8% for $n = 10$. Further checks were made with regard to the distribution of contact pressure under a frictionless indenter of flat, conical and spherical head-shape. The pressure distributions shown in Figs 5–7 for $n = 1$ and $\ell = 0$ are in excellent agreement with analytical solutions summarized by Johnson (1985).